

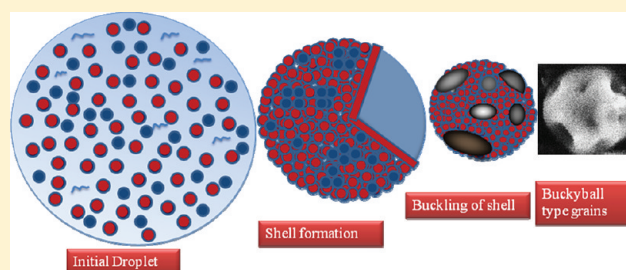
Control of Buckling in Colloidal Droplets during Evaporation-Induced Assembly of Nanoparticles

J. Bahadur,^{*,†} D. Sen,[†] S. Mazumder,[†] B. Paul,[‡] H. Bhatt,[§] and S. G. Singh^{||}

[†]Solid State Physics ([‡]Materials Processing, [§]High Pressure & Synchrotron Radiation Physics, ^{||}Technical Physics) Division, Bhabha Atomic Research Centre, Mumbai-400085, India

Supporting Information

ABSTRACT: Micrometric grains of anisotropic morphology have been achieved by evaporation-induced self-assembly of silica nanoparticles. The roles of polymer concentration and its molecular weight in controlling the buckling behavior of drying droplets during assembly have been investigated. Buckled doughnut grains have been observed in the case of only silica colloid. Such buckling of the drying droplet could be arrested by attaching poly(ethylene glycol) on the silica surface. The nature of buckling in the case of only silica as well as modified silica colloids has been explained in terms of theory of homogeneous elastic shell under capillary pressure. However, it has been observed that colloids, modified by polymer with relatively large molecular weight, gives rise to buckyball-type grains at higher concentration and could not be explained by the above theory. It has been demonstrated that the shell formed during drying of colloidal droplet in the presence of polymer becomes inhomogeneous due to the presence of soft polymer rich zones on the shell that act as buckling centers, resulting in buckyball-type grains.



1. INTRODUCTION

Recent advances in the area of self-assembly of nanoparticles (NPs) have encouraged the exploration of various synthesis techniques in fabrication of micrometer-sized grains with tailored morphology. In particular, anisotropic grains have been the subject of various studies in recent years. Such anisotropic micrometric grains can be obtained through different approaches, for example, either by deformation of spherical colloidal droplets during drying^{1–3} or by forming clusters of NPs.^{4–7} It has been demonstrated that such grains are potential candidates to generate anisotropic colloidal crystals.^{4,8,9} Hollow anisotropic grains are particularly interesting for a variety of applications such as drug delivery, catalysis, biotechnology, and contrast agents for ultrasound or echographic imaging.^{10,11} Microemulsion templated colloidal assembly^{12–17} and spray-drying^{18–26} are the most widely utilized techniques for fabrication of hierarchically structured micrometer sized grains. Recently, highly ordered nanostructured and hollow grains have been synthesized by using polystyrene colloids as template during spray-drying.^{27,28} During drying of a colloidal droplet, various physicochemical processes take place, which in turn decide the morphology of resulting dried/assembled grain. A viscoelastic shell of densely packed NPs forms at the surface of a drying colloidal droplet. Initially, the shell yields and gets thickened as the droplet shrinks. Later, the capillary forces that drive shell deformation overcome the electrostatic forces, stabilizing the colloidal particles. At a critical value of the capillary force, the particle undergoes a sol–gel transition, transforming the viscous shell

to an elastic solid, which triggers the onset of buckling. The parameter that decides the formation of the shell and the shell thickness is called the Peclet number (Pe). It is defined as the ratio of mixing time of the NPs in the droplet ($\tau_{\text{mix}} = R^2/D$, R is droplet radius, and D is diffusion coefficient of the NPs in the dispersion) to the drying time of the droplet (τ_{dry}). If Peclet number $Pe \gg 1$, the drying process is regarded as fast and there is a possibility of formation of hollow or doughnut/crumpled grains. However, if Peclet number $Pe \ll 1$, the drying process is regarded as slow and the droplet shrinks isotropically throughout the drying process, resulting in a uniformly jammed spherical grain. In our previous works, spray-drying experiments have been carried out in both the regimes, slow and fast, which led to spherical²⁹ and doughnut³⁰ grains, respectively. The origin of the buckled grains was attributed to the mechanical behavior of the elastic shell formed under capillary stress during drying of colloidal droplets.³⁰ Deformation of a spherical shell under external pressure has been investigated recently, both experimentally and numerically^{31–33} due to the pertinent engineering situations as well as the biomechanics. In this context, it is worthy to mention that the mechanical deformation of a thin elastic sheet of graphitic oxide,³⁴ polymerized Langmuir monolayer,³⁵ or cytoskeletons of biological membranes³⁶ has been well-studied in the past. However, curved shells exhibit quite different elastic behavior under external pressure because of the

Received: October 24, 2011

Revised: December 20, 2011

Published: December 20, 2011

coupling between stretching and bending effects.³⁷ This interplay between bending and stretching leads to a reduced flexibility of the shell.^{38–41} Some experimental and theoretical works^{42–49} show the complex geometry (i.e., wrinkled or dimpled sphere) of the grains due to buckling of shell formed during drying. The morphology of the spherical shell under external pressure is a result of the minimization of the energies due to extensional and bending deformations. For larger deformation, extensional deformation is not energetically favorable, and bending deformation is preferred. It is important to mention here that for small deformations, the potential energy of buckling is higher as compared to that of no buckling. However, the potential energy for the buckled state is lower as compared to that of the nonbuckled state for larger deformation.⁴⁵ It has been shown that for a homogeneous spherical elastic shell, two modes of deformation may be combined by the Föppl–von Kármán (FvK) number γ . Recently, it has been shown by simulations that the higher γ coupled with high rate of compression may lead to multiple numbers of the indentations on the shell, leading to the buckyball type of morphology.^{43–45} The elastic shell formed during drying of colloidal droplet in the fast drying regime may be treated as an experimental model for the shell under external pressure. Peclet number Pe and the capillary pressure on the shell decide the rate of compression and the h/R_c ratio. It is interesting to note that the nature of the shell buckling can also be controlled by altering the pressure on the shell or by introducing inhomogeneity in the shell. To the best of our knowledge, this aspect of the controlled buckling has not been dealt experimentally so far and calls for further experimental as well as numerical investigations. In real systems, spherical shells are not always homogeneous such as in engineering materials, soft materials, or living cells, etc. They always possess some degree of inhomogeneity. The effect of shell inhomogeneity on the buckling phenomenon has not been well studied because of its complexity and needs attention.

In the present work, it has been shown that the shell inhomogeneity plays an important role in inducing the buckling of the shell formed during drying of droplet. Buckling of the drying colloidal droplets has been controlled by modifying silica colloids using poly(ethylene glycol) (PEG) of different molecular weights and concentrations. Small-angle neutron scattering (SANS) and scanning electron microscopy (SEM) experiments have been performed to probe the hierarchical length scales of the assembled grains. Thermogravimetric analysis (TGA) and infrared (IR) spectroscopy experiments have been performed to monitor the removal of the polymer from assembled grains. In this paper, the origin of the doughnut, spherical, and buckyball type of grains has been investigated in the light of shell-buckling theory. It will also be shown that the origin of the buckyball-like grains, in present case, is because of shell-buckling during drying and not due to templating by the polymer.

2. EXPERIMENTAL METHODS

Spray-drying experiments have been performed on stable 2 wt % silica colloidal dispersion (Visa Chemicals, Mumbai, India) using a spray dryer (LU 228⁵⁰) having two fluid atomizer nozzle. PEG of molecular weights 400 (PEG400) and 1450 (PEG1450) were obtained from Sigma Aldrich; 0.5, 1.0, 2.0, and 3.0 g of PEG400 were mixed one by one with 100 mL of 2 wt % silica colloids and stirred well. Similarly, 0.5, 1.0, 2.0, and 6.0 g of PEG1450 were mixed with 2 wt % silica colloids. These stable dispersions were spray-dried at an atomization pressure of 2.0 kg/cm² and inlet temperature at 170 °C. The solution feed rate was kept as 2 mL/min and the aspiration rate was fixed

at 50 m³/h. The spray-dried powder specimens were calcined at 500 °C for 4 h in order to remove the polymer from the assembled grains. Samples, obtained from spray-drying of dispersion containing PEG400 are designated as S1 in general. Further, specimens obtained for different weight percent of PEG400 are named as S1pt5, S1p1, S1p2, and S1p3 for 0.5, 1.0, 2.0, and 3.0 wt %, respectively. Similarly, specimens, obtained from spray-drying of dispersion containing PEG1450 are designated as S2pt5, S2p1, S2p2, and S2p6 for 0.5, 1.0, 2.0, and 6.0 wt %, respectively (S2 in general). The drying experiments could not be performed beyond 3 wt % PEG400 concentration due to the sticky nature of the grains, which hindered the collection of the powder from the cyclone separator of the spray dryer. The concentration of PEG1450 could not be increased beyond 6 wt % for the same reason as mentioned above. The mesoscopic characterization of the samples has been carried out by SEM. The micrograph of the grains, obtained for 2 wt % silica only, is shown in Figure 1. Micrographs of calcined specimens for S1 and S2 specimens are shown in Figure 2 and 3, respectively.

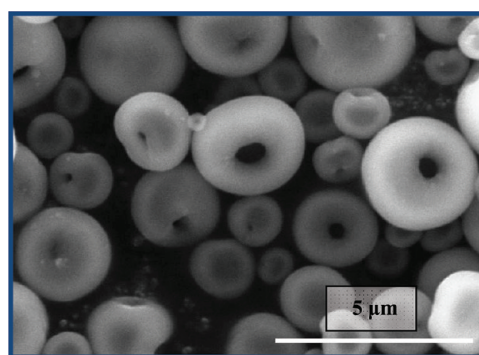


Figure 1. SEM micrograph of the self-assembled grains obtained for drying of only 2 wt % silica dispersion.

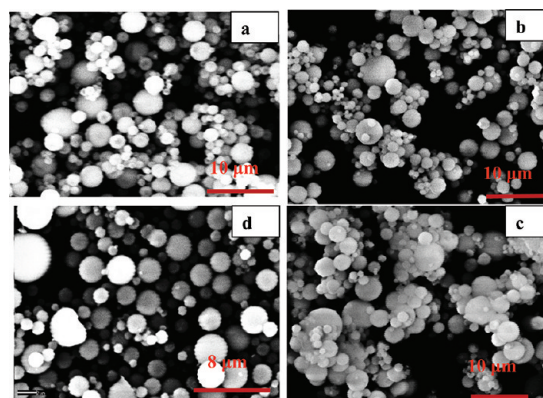


Figure 2. SEM micrographs of calcined specimens of (a) S1pt5, (b) S1p1, (c) S1p2, and (d) S1p3.

IR spectroscopy has been performed on assembled grains before and after calcinations in order to probe the nature of functional groups of polymer and silica NPs in addition to ascertain the release of polymer after calcination. Infrared spectra of the powders were recorded in the spectral range 400–4000 cm⁻¹ using a Bruker Vertex 80 V FTIR spectrometer under the vacuum condition, at an apodized resolution of 2 cm⁻¹. The spectrometer was configured with globar source, KBr beamsplitter, and deuterated triglycine sulfate (DTGS-Mid IR) detector. For recording the infrared spectrum, powders have been pelletized with samples dispersed in KBr matrix. Background spectrum using bare KBr pellet has been divided in each case to obtain the absorbance spectrum, denuded from instrumental and

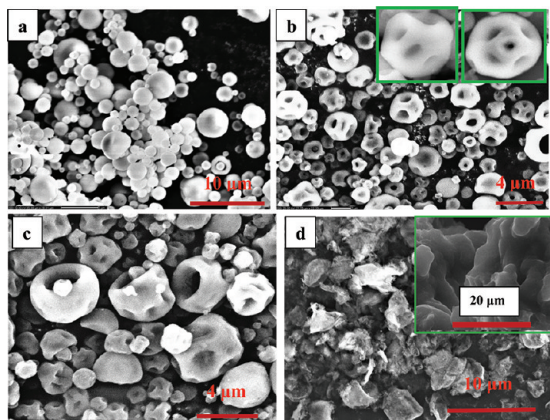


Figure 3. SEM micrographs of calcined specimens of (a) S2pt5, (b) S2p1 (left and right inset show buckyball grains before and after calcinations, respectively), (c) S2p2, and (d) S2P6 (inset shows the micrograph of noncalcined S2P6 specimen).

environmental profiles. The IR spectra for S1 specimens before and after calcinations are shown in Figures 4 and 5, respectively. IR spectra

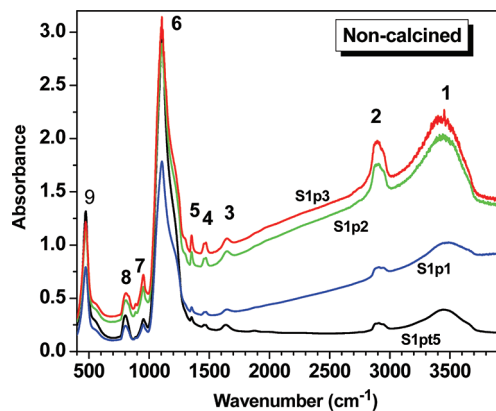


Figure 4. Infrared spectra of the noncalcined grains with varying concentration of PEG400. The characteristic IR modes are numbered and are listed in Table S1 of the Supporting Information.

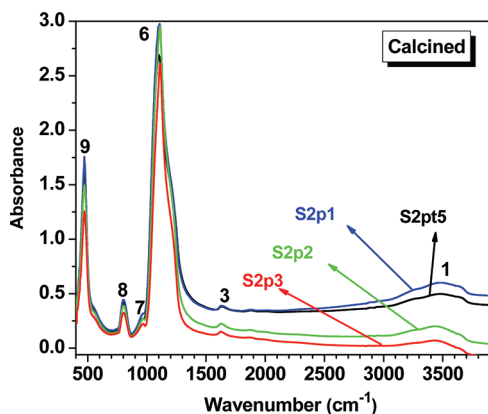


Figure 5. Infrared spectra of the calcined grains with varying concentration of PEG400. The characteristic IR modes are numbered and are listed in Table S1 of Supporting Information.

for S2 samples, before and after calcinations, are shown in Figures S1 and S2 in the Supporting Information.

Removal of polymer from the assembled grains has also been monitored by TGA and differential thermal analysis (DTA). The DTA data were recorded in ambient air at a uniform heating/cooling rate of $5\text{ }^{\circ}\text{C min}^{-1}$ up to a maximum temperature of $500\text{ }^{\circ}\text{C}$ in each experiment employing the SETARAM TG-92 system. The TGA signal was recorded using a microgram scale having $0.1\text{ }\mu\text{g}$ as the least count for the same temperature range. The TGA–DTA curves for the removal of PEG400 and PEG1450 polymers from the assembled grains are shown in Figures 6 and 7, respectively.

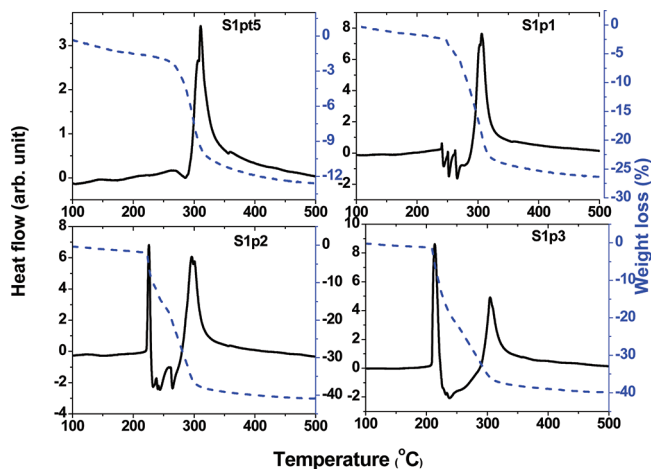


Figure 6. Heat flow and weight loss curves for spray-dried grains for varying PEG 400 concentrations.

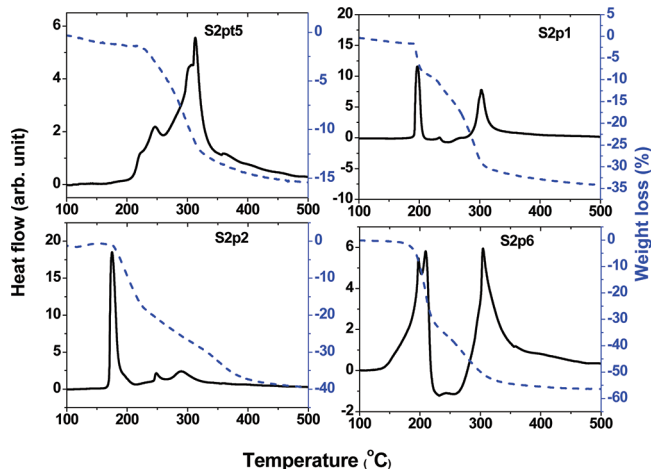


Figure 7. Heat flow and weight loss curves for the spray-dried grains for varying PEG1450 concentrations.

Preliminary measurements with medium-resolution small-angle neutron scattering (MSANS)⁵¹ on spray-dried grains have indicated two levels of structural hierarchy in the grains. Further, SANS experiments have also been performed on KWS1⁵² and KWS3⁵³ instruments at the high flux reactor FRM-II (Garching, Germany) to collect data over a wide scattering vector (q) range with improved statistics and resolution. Since, the SANS experiments have been performed on the powder samples, it is well-known that it is difficult to convert the intensity scale into an absolute scale, although it has been shown earlier⁵⁴ that effective thickness may be obtained in such a case if the exact composition and density of the powder sample is obtained. Also, it is to be noted that data analysis has been carried out only for calcined samples where PEG is removed from assembled silica grains. Further, the amount of silica in calcined grains has been kept identical for all the samples. Thus, normalization of the data at the high q region has been done where scattering contribution from silica particles is

dominant. It is to be mentioned that the normalization of the SANS profiles of the calcined specimens has been performed at $q = 0.72 \text{ nm}^{-1}$ in order to compare the functionality of the scattering profiles. It is primarily based on two reasons. First, the size of the silica NPs remains the same for all the calcined specimens. Hence, the functionality of the form factor for the silica particle remains the same at high q . Second, the effect due to interparticle interference is insignificant at higher q . It is to be mentioned that the normalization of profiles may also be done at any other q value at higher q for the above purpose. The SANS profiles were corrected for instrumental resolution and incoherent scattering. SANS profiles for calcined S1 and S2 specimens are shown in Figures 8 and 9, respectively.

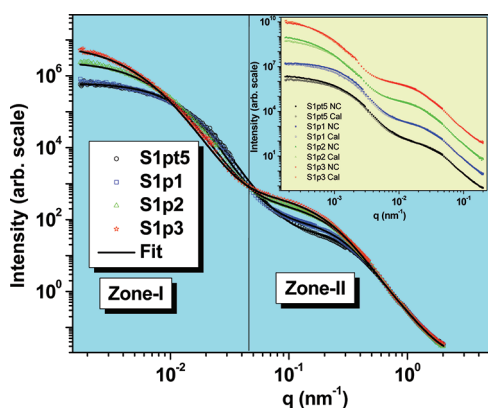


Figure 8. Normalized SANS profiles of calcined assembled silica grains obtained for different PEG400 concentrations (S1) are shown. The solid lines are a fit of the model to the data. The inset shows SANS profiles for noncalcined and calcined samples for varying PEG400 concentration. The profiles in the inset have been scaled vertically for clarity. Noncalcined and calcined specimens are abbreviated as NC and Cal, respectively.

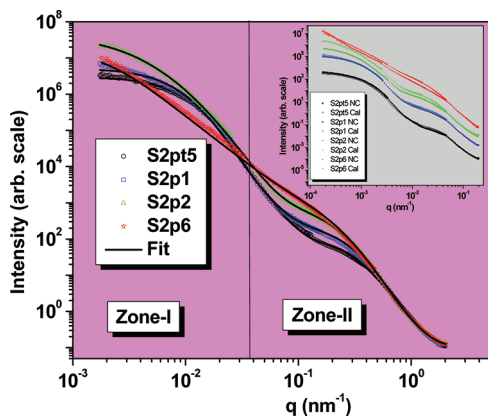


Figure 9. Normalized SANS profiles of calcined assembled silica grains obtained for different PEG1450 concentrations (S2). The solid lines represent the fit of the model to the data. The inset shows SANS profiles for noncalcined and calcined samples for varying PEG1450 concentration. The profiles in the inset have been scaled vertically for clarity. Noncalcined and calcined specimens are abbreviated as NC and Cal, respectively.

3. RESULTS AND DISCUSSION

From the SEM micrographs (Figure 1), it is evident that grains obtained from spray-drying of only 2 wt % silica colloids possess doughnut morphology. However, the grains obtained from dispersion modified by PEG400 possess spherical

morphology, as depicted in Figure 2. It is found from Figure 2a that spherical grains with a small dimple have been observed for the S1pt5 specimen. This dimple disappears when the PEG400 concentration is increased to 1, 2, and 3 wt %. Spherical grain morphology without a dimple has been observed for S2pt5 (Figure 3a). As PEG1450 concentration is increased further to 1 wt %, the morphology of the grains undergoes a shape transition from spherical to buckyball (Figure 3b). The morphology of the grains has well-defined multiple indentations on a nearly spherical matrix. Similar grain morphology has also been observed for S2p2 specimens with an increase in the size of the indentations (Figure 2c). Collapsed grains having spongelike morphology have been obtained when the PEG1450 concentration is increased to 6 wt % (Figure 2d). The SEM micrographs in Figures 1 and 2 were analyzed for their typical size by ImageJ software. The typical grain size, estimated by image analysis of the electron micrographs for S1 and S2 specimens, are tabulated in Tables 1 and 2. It is important to mention here that noncalcined S1 and S2 specimens were also characterized by SEM. It was observed that SEM micrographs of the calcined and noncalcined grains are identical, except for a small variation in overall grain size.

It is discernible from Figure 4 that IR spectra bear the signature of the organic group $-\text{CH}-$ in addition to the characteristic modes of silica. The approximate positions of the different modes and their assignment to a functional group (based on the literature)^{55–57} are depicted in Table S1 of the Supporting Information. IR spectra of the calcined S1 specimens are shown in Figure 5. It is evident that IR modes related to $-\text{CH}-$ groups are not present in the samples after calcinations at $500 \text{ }^\circ\text{C}$ for 4 h. However, bending and stretching modes of $-\text{OH}$ groups are still present in the samples that are calcined at $500 \text{ }^\circ\text{C}$. The origin of the broad $-\text{OH}$ stretch peak, centered around 3450 cm^{-1} in calcined specimens, may be attributed to the contribution from various $-\text{OH}$ groups, such as silanol groups on the silica surface and bound waters in the interstices of the jammed silica NPs. Similar results have also been observed for S2 samples. It has also been observed that the relative absorption corresponding to $\text{Si}-\text{OH}$ functional group decreases after calcination, indicating the reduction of $\text{Si}-\text{OH}$ functional groups on silica NPs during heat treatment. The IR spectra of the noncalcined and calcined S2 samples are shown in Figures S1 and S2 of the Supporting Information.

It is observed that heat flow and weight loss curves for S1 and S2 grains are quite different. From Figure 6, it is found that for S1pt5 and S1p1 specimens an exothermic peak appears nearly at $300 \text{ }^\circ\text{C}$ due to calcination of PEG. Some weaker endothermic peak like structures are also observed before this exothermic peak. When the concentration of PEG400 is increased to 2 and 3 wt %, an extra exothermic peak appears at relatively lower temperature. This exothermic peak is not preceded by any endothermic peak. It is known that removal of the trapped and free polymer shows different thermogravimetric behavior.⁵⁸ Free polymers manifest an exothermic peak at relatively low temperature. However, for trapped polymers, an exothermic peak appears at relatively higher temperature, as it requires a larger amount of energy for dissociation. The presence of an endothermic peak before the exothermic peak due to trapped polymers indicates that some amount of heat is required to desorb the attached polymers. A smaller endothermic peak indicates the noncovalent nature of interaction between silica and the polymer. In the present case, the polymers may get attached on silica NPs via

Table 1. Fitting Parameters Obtained from SANS Data Analysis for Calcined S1 Specimens

specimen (calcined)	structure factor $S(q, \Phi)$ parameters due to jammed silica NPs		pore size distribution parameters templated by free PEG aggregates		overall grains size distribution parameters			Guinier radius, R_g (nm)	grain size by image analysis (μm)	C_1/C_2 ($\times 10^{-3}$)
	stickiness parameter, τ	volume fraction, Φ	average radius (nm)	polydispersity, σ	average radius, r_g (nm)	polydispersity, σ				
S1pt5	0.2	0.58	no contribution		76	0.45	257 ± 30	1.1 ± 0.6	9.54	
S1p1	0.2	0.49	no contribution		94	0.41	263 ± 37	1.9 ± 0.9	4.70	
S1p2	0.2	0.49	5.2	0.42	114	0.50	401 ± 14	1.5 ± 0.8	4.89	
S1p3	0.2	0.49	6.4	0.40	128	0.55	488 ± 10	2.2 ± 1.1	2.08	

physisorption or through hydrogen bond because of the presence of the $-\text{OH}$ groups on the silica colloids. The weight loss curves during the removal of polymer show a consistent behavior with the calculated weight loss. Weight loss curves also show one or two slopes according to the appearance of one or two exothermic peaks in the heat flow curve. Figure 7 shows the thermogravimetric behavior of the S2 grains. It is evident that the exothermic peak due to free PEG1450 appears even at 1 wt % concentration, while the appearance of an exothermic peak in the case of PEG400 was at 2 wt %.

The TG analysis and IR spectra of the PEG incorporated grains provide crucial information regarding the interaction of PEG and silica NPs. While IR indicates the presence of the $\text{Si}-\text{OH}$ functional groups on its surface even after calcinations at 500°C , the heat flow curves indicate the existence of both trapped as well as free polymers in the assembled grains. On the basis of these results, it is believed that PEG interacts with the silica NPs via $\text{Si}-\text{OH}$ groups and gets absorbed on silica NPs. These polymer-covered NPs get assembled in a random jamming process during drying of the droplet. Thus, coated polymers in this case are trapped between the interstices of the jammed NPs and manifest an exothermic peak at higher temperature. When the concentration of the polymers is increased to higher weight percent, absorption of polymer on NPs gets saturated and additional PEG polymers become free and may also form smaller aggregates. It is also evident from the heat flow curve that for high molecular weight polymer, free polymer appears at lower concentration as compared to that of low molecular weight polymer. It shows that the absorption of polymer on NPs saturates at lower concentration for higher molecular weight.

It is worth mentioning that microscopy is a direct but local probe and thus does not provide statistically averaged information. Nevertheless, it is an important complementary technique to scattering results. SANS provides statistically averaged information over the mesoscopic length scale. The SANS profiles of calcined S1 and S2 specimens are depicted in Figures 8 and 9, respectively. Scattering profiles showing the effect of calcinations of the grains containing PEG400 are depicted in the inset of Figure 8. It is discernible that calcination modifies SANS profiles at very low q region. Guinier analysis of the scattering profiles shows that the size of grains decreases slightly after calcination. The image analysis of the electron micrographs for the grains before and after calcinations also supports this observation. From the inset of Figure 9, it is observed that scattering profiles of calcined and noncalcined specimens for both S2pt5 and S2p1 approximately match. However, the scattering profiles for S2p2 and S2p6 specimens differ slightly in scale before and after calcination except at higher q ; however, their functionality remains more or less similar, indicating almost similar morphology except the change in contrast due to removal of PEG.

It is evident from Figures 8 and 9 that a wide q range enables us to examine two level structures of the grains. The scattering profiles may be broadly divided into two zones mainly. The scattering contribution from overall grains is centered predominantly in zone I. The information on the smaller entities, i.e., the assembled NPs, is primarily dominant in zone II of the scattering profiles. Similar observations also follow for S2 grains. However, this is not true for the S2p6 specimen, as we will discuss later. It is interesting to note that simple addition of scattering contributions from different entities may be approximated by additive terms if their length scales differ widely. The scattered intensity from two level structure is modeled as $I(q) = I_1(q) + I_2(q)$, where $I_1(q)$ is the scattering contribution from overall grains and $I_2(q)$ is the scattering contribution from the packed silica NPs within the grains.

It is evident from SEM micrographs that the grains are spherical in nature for the S1 specimens. The grains for S2pt5 are spherical, and grains for S2p1 and S2P2 are deformed spheres. Hence, the scattered intensity from the overall grains $I_1(q)$ is modeled in the light of polydisperse spheres, $I_1(q) = C_1 \int P(q,r) r^6 D(r, r_{0g}, \sigma_g) dr$, where $P(q,r)$ is the form factor of a sphere of radius r and may be written as⁵⁹ $P(q,r) = 9 \{ [\sin(qR) - qR \cos(qR)] / (qR)^3 \}^2$. It is to be noted that the scattering intensity depends on the square of the volume of the inhomogeneity. For a system of polydisperse spheres, the square of volume term (r^6) has been taken inside the integration. All other r independent terms are absorbed in the coefficient C_1 . $D(r, r_{0g}, \sigma_g)$ is the log-normal size distribution with median grain radius r_{0g} and the polydispersity index σ_g . The expression for the log-normal size distribution having median size r_0 and polydispersity index may be written as⁶⁰ $D(r, r_0, \sigma) = [1 / (2\pi\sigma^2 r^2)^{1/2}] \exp\{-[\ln(r/r_0)]^2 / 2\sigma^2\}$.

The average radius of grains $\langle r_g \rangle$ can be expressed as $\langle r_g \rangle = r_{0g} \exp(\sigma_g^2/2)$. The volume weighted averaged grain size distribution for S1 and S2 specimens are depicted in Figure 10 and its inset, respectively. It is interesting to note that the effect due to the correlation between the overall grains is expected to be manifested at very low q . It is evident from Figures 8 and 9 that SANS profiles are not significantly affected by the correlation between overall grains in the present accessible q regime. However, one can explore the effect of correlation between grains by accessing the further lower q by static light scattering experiments.

The expression for $I_2(q)$ may be written as the following if an interacting polydisperse spherical particle model is assumed under local monodisperse approximation:⁶¹ $I_2(q) = C_2 \int P(q,r) r^6 D(r, r_{0np}, \sigma_{np}) S(q, \tau, \Phi) dr$, where $D(r, r_{0np}, \sigma_{np})$ is the log-normal size distribution of jammed silica NPs with a median radius r_{0np} and polydispersity index σ_{np} . $S(q, \tau, \Phi)$ is the structure factor and is assumed to be a sticky hard sphere type with τ as the inverse stickiness parameter and Φ as the local packing fraction of the NPs.⁶² The expression of the $S(q, \tau, \Phi)$ is quite complex and can be

Table 2. Fitting Parameters Obtained from SANS Data Analysis for Calcined S2 Specimens

specimen (calcined)	structure factor $S(\tau, \Phi)$ parameters due to jammed silica NPs		pore size distribution parameters templated by free PEG aggregates		overall grains size distribution parameters		Guiner radius, R_g (nm)	grain size estimated by image analysis (μm)	C_1/C_2 ($\times 10^{-5}$)	
	stickiness parameter, τ	volume fraction, Φ	average radius (nm)	polydispersity, σ	average radius, r_g (nm)	polydispersity, σ_g				
S2pt5	0.2	0.60	no contribution	94	0.44	311 \pm 30	1.67 \pm 0.8	7.387		
S2p1	0.2	0.50	4.4	0.39	105	0.45	380 \pm 15	1.9 \pm 0.7	8.33	
S2p2	0.2	0.50	7.3	0.34	114	0.50	482 \pm 11	2.1 \pm 1.0	33.4	
specimen (calcined)	lower cutoff, r_w (nm)	fractal dimension, D_F	upper cutoff, ξ (nm)	polydispersity, σ	average radius (nm)	polydispersity, σ	Guiner radius, R_g (nm)	grain size estimated by image analysis (μm)		
S2p6	11.8	2.4	495	0.34	3.41	3.41	566 \pm 24	—		
	pore size distribution parameters templated by free PEG aggregates									

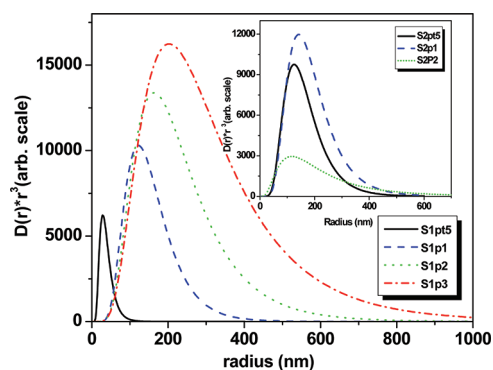


Figure 10. The grain size distributions for the S1 sample series as obtained from the SANS analysis. Inset shows grain size distributions for S2 samples obtained from the SANS analysis except S2p6.

retrieved from the literature.^{62–64} It is found that neither the exact hard sphere repulsive interaction nor the fractal correlation could fit the data well. At the same time, a sticky hard sphere model produces a better agreement. Jamming behavior during drying of a colloidal droplet gives an exact idea about the interaction between jammed NPs. During drying of a colloidal droplet, the NPs come closer because of the attractive capillary force and finally get trapped in van der Waal type of potential well at the end of drying. The nature of the van der Waal potential between locked NPs may be approximated as a sticky hard spheres interaction type. The above two level structures model is successful to fit the scattering profiles for S1pt5 and S1p1. The scattering profiles of S1p2 and S1p3 could not be fitted by realistic parameters without considering extra scattering contribution in zone II (as scattering in zone II is increasing with increasing polymer concentration), which in fact originates from the templated pores from the PEG aggregates. Similarly, the scattering profiles for the S2pt5, S2p1, and S2p2 could not be modeled using the above-mentioned two level structures model. The scattering contribution due to PEG templated pores may be written as $I_3(q) = C_3 \int P(q,r) r^6 D(r, r_{0\text{pore}} \sigma_{\text{pore}}) dr$.

The existence of such small pores is evident from the existence of free PEG aggregates in noncalcined samples through TGA. It is to be noted that the size of PEG templated pores is comparable to silica NPs size and hence should not be confused with the hole size of the buckyball, as their size is on the order of a micrometer. At this juncture, it is important to mention that in present data analysis, the scattering contribution from smaller pores [$I_3(q)$] is simply added to the scattering contribution from NPs [$I_2(q)$]. There may be some effect due to avoidance of cross terms which may arise due to similar length scale of NPs and pores. However, for simplicity and also to reduce the number of parameters in fitting, the above approximation is adopted.

It is to be noted that the silica NPs size distribution was kept fixed during analysis of SANS data for all the calcined specimens, as the size of the NPs in the initial colloids remains the same. The NPs size distribution $D(r, r_{0\text{np}} \sigma_{\text{np}})$ is shown in Figure S3 of the Supporting Information. The average radius of the silica NPs is found to be 5.8 nm with polydispersity index 0.43. Although, the size distribution of the NPs remains constant, the local packing fraction (Φ) of NPs does not remain constant at the higher weight fraction of PEG. For S1pt5 grains the local packing fraction (Φ) of NPs is 0.60. The local packing fraction decreases to 0.50 when PEG400 concentration is increased to 1 wt %, and it remains constant for higher concentration. The pore size distribution, as

estimated by SANS analysis, is depicted in Figure 11. It is evident from Figure 11 that the typical size of the PEG

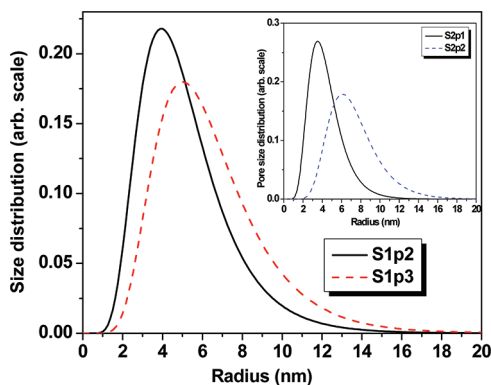


Figure 11. Pore size distributions for S1p2 and S1p3 calcined specimens, as obtained from the SANS analysis. Inset shows the pore size distributions for S2p1 and S2p2 specimens.

templated pores is 10 nm; hence, these pores cannot be seen in SEM micrographs due to resolution limitations. Similarly, local packing fraction Φ of NPs was nearly 0.60 for S2pt5 specimens. When the concentration of PEG1450 is increased to 1 wt %, Φ decreases to 0.5 and it remains constant at higher concentrations. The pore size distributions for S2 specimens are shown in the inset of Figure 11. The value for C_1/C_2 has been estimated for each specimen. We have observed a decreasing trend in the ratio of the C_1/C_2 in the S1 specimens. Actually, an attempt has been made to understand the trend in terms of the compactness of the grains. It is important to note that the polydisperse solid sphere model was adopted in fitting the scattering contribution from the grains. However, if the grains would have been true solid sphere in all cases, then the ratio C_1/C_2 should have remained constant. The decrease in the ratio of C_1/C_2 is attributed to the decrease in the compactness of the grains. The C_1/C_2 ratio for untreated assembled silica grains was found to be highest with a value 13.8×10^{-5} .

The other ratios, such as C_3/C_2 and C_{fractal}/C_3 , were also estimated, but these ratios could not provide conclusive information regarding grain morphology.

It is worth mentioning that the SANS profile for S2p6 specimen is entirely different. In this case, the scattering profile follows power law behavior over a wide q range. The correlation of the assembled NPs is modified from sticky hard sphere interaction to a fractal type of interaction. The scattered intensity has been modeled as follows:

$I(q) = I_{\text{fractal}}(q) + I_3(q)$, where $I_{\text{fractal}}(q) = C_{\text{fractal}} \int D(r, r_{\text{onp}}, \sigma_{\text{np}}) r^6 P(q, r) dr S(q, r_{\text{av}}, \xi)$ and $S(q, r_{\text{av}}, \xi)$ is the fractal structure factor and is expressed as

$$S(q, r_{\text{av}}, \xi) = 1 + \frac{1}{(qr_{\text{av}})^{D_F}} \frac{D_F \Gamma(D_F - 1)}{\left[1 + \frac{1}{q^2 \xi^2}\right]^{(D_F - 1)/2}} \sin[(D_F - 1) \tan^{-1}(q\xi)]$$

where r_{av} and ξ are lower cutoff (average NPs size) and upper cutoff lengths of the fractal structure, respectively. D_F is the fractal dimension and describes the nature of the correlation of the NPs in the aggregate. The ratios C_1/C_2 for S2 specimens do not follow any kind of trend because of the significant deviation of its shape from a sphere. To avoid the complexity and also to

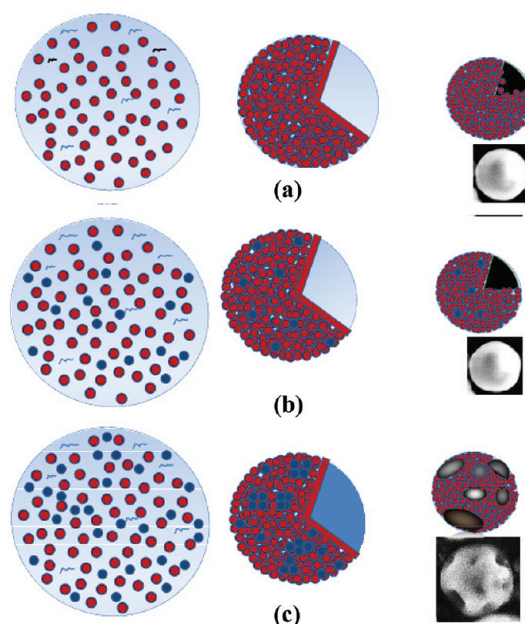
reduce the number of fitting parameters, the shape polydispersity is not accounted for in the present model of SANS analysis. It is to be noted that the ratios C_{fractal}/C_3 were also estimated, but they do not provide any conclusive information.

The parameters obtained from SANS analysis for PEG400 and PEG1450 are tabulated in Tables 1 and 2, respectively. It is observed from the tables that there is a difference in size of the grains obtained from SEM micrographs and SANS analysis. This arises primarily due to two reasons. First, SEM is a local probe of materials. The information, extracted by the image analysis of the micrographs, may not be adequately statistically averaged, as it is based on counting of fewer grains. Smaller grains, which are not observed from SEM, remain uncounted as far as image analysis is concerned. However, SANS is a bulk probe of the matter and gives statistically averaged information on the distribution of the grains. Further, the polydispersity of the grains is also significant. Second, the SANS data has been recorded in limited q regimes. The scattering contribution from large enough grains may not be significant in the present experimental q range. However, the qualitative trend in the variation of grain size, as obtained by SEM, Guinier analysis, and model fitting of whole profiles, corroborate each other. At this juncture, it is important to mention that the model is complex enough to extract information on the buckyball-type holes and grains separately, as the grains are significantly polydisperse for S2p1 and S2p2. The scattering contributions from the buckyball holes in the grains and smaller grains may overlap in the same q region and are difficult to separate. This might have led to somewhat of an underestimation of the actual grain size.

Recently, the origin of the doughnut morphology of grains during drying of bare silica colloids in fast drying regime has been elucidated.³⁰ It was observed that buckling of the shell formed during drying gives rise to doughnut morphology. Dimensionless Peclet number Pe has been estimated to be ~ 3.5 for the present drying conditions for 2 wt % silica colloid, which indicates that drying comes under the fast drying regime.³⁰ The formation of the shell of NPs during evaporation-driven assembly plays an important role in deciding the final morphology of the self-assembled grain. As mentioned earlier (Figure 1), only the grains for 2 wt % silica colloids possess doughnut morphology. However, spherical morphology is achieved on just addition of PEG400 polymer in 2 wt % silica colloids. Slightly dimpled spherical morphology is observed for S1pt5 specimens. The arrest of the buckling phenomenon on addition of PEG400 polymer may be understood as follows. During drying of the colloidal droplet, evaporation brings the NPs into the liquid–water interface, where their concentration grows. In contrast, in the core of a droplet, the volume fraction of the NPs remains approximately equal to its initial value. This accumulation thus leads to the formation of a boundary layer through which the concentration changes. As time passes, two effects occur. The concentration at the shell increases and the boundary layer becomes thicker. When the concentration reaches the gel concentration value (~ 0.6), a characteristic of the close packing of particles, a gelled shell forms at the surface. As evaporation continues, the drop progressively flattens. As water evaporates, tiny menisci form in the gaps between particles at the surface of the shell. The pressure difference across the menisci is $2\gamma/r_M$ (capillary pressure), where r_M is the local radius of curvature. This capillary pressure drives the deformation of the shell. Stress on the shell due to capillary pressure may be controlled by the modification of the colloidal particle size. However, a critical pressure $p_c = 4Y_0(h/R_c)^2$ is required to induce the buckling of a homogeneous shell.⁴⁴ If the stress due to capillary pressures exceeds the critical pressure, the formed shell buckles.

As observed from Figure 1, the buckled grains with a single indentation (doughnut grains) has been observed for the case with only silica colloids. When the PEG is added to silica colloids, it interacts with the silica NPs via hydrogen bond and gets adsorbed on the NPs to form a coating. Due to polymer coating, silica NPs could not come closer as compared to that in the case of only silica NPs case. Thus, the local menisci radius r_M is relatively large in this case, resulting in smaller capillary pressure, which is not sufficient to induce the buckling during drying of the droplet. For 0.5 wt % of PEG400, buckling of the shell is not fully arrested and dimpled grains are observed. However, coating of the polymers on NPs increases when the concentration is increased to 1 wt %, leading to the lower packing fraction of NPs in the calcined grains, as was observed from SANS analysis. Thus, an increase in the coating amount on NPs leads to further reduction of capillary pressure, resulting in spherical grains without any dimples. If the concentration of the PEG400 is increased further to 2 and 3 wt %, the coating of the polymer saturates and free polymers in the form of aggregate result, in addition to the coated polymers, as is supported by the TGA–DTA curve. SANS data of the calcined samples indicate the presence of the pores which was templated by free PEG aggregates. The size of PEG aggregates was similar to that of NPs size (~ 10 nm). Since the size of the PEG aggregates is similar to that of the silica NPs size, they became the part of the shell that is formed during the assembly process of colloids in the drying droplet. Thus, the shell in this case is not homogeneous. However, for small molecular weight polymer (PEG400) the number of aggregates is not significant, even for 3 wt %. If the molecular weight of the PEG is increased from 400 to 1450 (approximately 4 times) free PEG appears even at 1 wt %. It was observed from the SEM micrographs that the assembled grains of S2p1 and S2p2 are of buckyball-type morphology, which is quite an intriguing observation. As discussed earlier, addition of PEG400 reduces the buckling due to a coating of polymers on NPs. However, in the case of S2p1 and S2p2 specimens the buckyball type of grains have been observed due to increased buckling of the shell. It is to be noted that the addition of polymer of low molecular weight, as in the present case, does not modify the viscosity of the initial dispersion significantly.⁶⁵ Also, the drying parameters remained identical for both cases, i.e., for only silica colloid and polymer-treated colloid. An attempt has been made to understand the origin of the grain morphology having multiple indentations in view of the theory of homogeneous spherical elastic shell. It has been discussed earlier that the relative thickness of the shell (h/R_c) and the rate of deformation decide the degree of the buckling or the number of indentations during drying for a homogeneous elastic shell. Since the drying parameters and dispersion properties are not altered significantly on addition of polymer, it is expected that the rate of deformation and relative shell thickness should not change significantly. It was argued earlier that the capillary pressure on the shell decreases on addition of polymer. Also, the relative shell thickness (h/R_c) may increase on addition of polymer due to coating of silica NPs and the presence of the free PEG aggregates on the shell at higher concentration. This will lead to lower γ value and smaller external pressure as compared to those for the unmodified silica colloids case. Thus, according to the elastic homogeneous spherical shell theory, buckling should have been arrested in the case of S2p1 and S2p2 specimens. Hence, in the present scenario, the theory of homogeneous elastic spherical shell fails to explain the origin of the buckyball-type morphology for the S2p1 and S2p2 specimens. However, if inhomogeneity on the shell is invoked, the present experimental observation may be explained satisfactorily. An elastic shell, formed during assembly, will comprise

both silica and soft PEG aggregates, as they are of comparable sizes. In this process, the shell becomes inhomogeneous as far as the shear modulus is concerned. It is important to mention that deformation of the shell under external pressure also depends on the Young modulus of the shell. If the Young modulus is smaller, the induced deformation is larger. The PEG aggregates on the surface of the shell act as the center for the buckling under capillary pressure. Also, the critical pressure for this kind of inhomogeneous shell will be lower as compared to that of the homogeneous shell of silica. The zones with soft components of the shell will be buckled at relatively smaller capillary pressure. It was observed that although free PEG aggregates in case of S1p2 and S1p3 are available, the number of aggregates will be smaller as compared to that for S2p1 and S2p2 due to higher molecular weight. Thus, buckling could not be induced for the shell having fewer PEG aggregates on the shell. It is to be mentioned that, in present case, the size of the PEG aggregates (~ 10 nm) is significantly smaller as compared to the size of the buckyball holes ($\sim 1 \mu\text{m}$) in the grains. So, buckyball holes in the grains cannot be due to mere templating of PEG aggregates of size 10 nm. Hence, the origin of such buckyball holes on the grains is attributed to buckling of an inhomogeneous shell as PEG aggregates of 10 nm make the shell inhomogeneous during drying. It needs to be mentioned that the buckyball-like grains may also be synthesized by using bigger polymer colloids, like polystyrene under nonbuckling regime, where buckling of the shell does not occur during drying.^{27,28} However, the size of polystyrene colloids should be comparable to the buckyball holes in the templating method unlike the present case. This also becomes evident from the SEM micrograph (inset of Figure 3c) that such buckyball holes are present even in the noncalcined grains. A schematic regarding the mechanism for the origin of the buckyball type grains has been depicted in Figure 12.



Initial colloidal droplet Shell formed during drying Final grain morphology

Figure 12. The schematic shows three different stages of drying (a) silica colloids coated with polymer and no PEG aggregate, (b) silica colloids coated with polymer and PEG aggregates are small in number (size of the PEG aggregates is 10 nm), (c) silica colloids coated with polymer and PEG aggregates are larger in number (size of the PEG aggregates is 10 nm). Note that buckyball holes do not arise due to PEG aggregates but result due to shell buckling.

To see the effect of further higher concentration of PEG1450, spray-drying experiment has been performed on silica colloids modified with 6 wt % polymer. It is observed from Figure 3d that spongelike grains are observed. The SEM micrograph of the noncalcined S2p6 specimen shows the grains are collapsed into each other (inset of Figure 3d). It is also observed from SANS data that a fractal-like correlation between the silica NPs exists over two decades of the length scale. The SANS data also show the presence of the pores templated by PEG aggregates. This result also indicates that the concentration and molecular weight of PEG polymer are key parameters to tune the buckling phenomenon in this system.

4. CONCLUSIONS

It has been shown that the phenomenon of morphological transformation to doughnut-like shape during drying of droplets containing a single type of colloid can be comprehended in terms of buckling theory of a homogeneous elastic shell. Further, such buckling phenomenon could be arrested by covering the NPs by PEG. The buckyball-type morphology of the grains could be realized due to buckling at higher molecular weight and concentration of the polymer. SANS results show the existence of PEG aggregates, which are much smaller than the dimples in the buckyball-type grains, at higher polymer concentration. The origin of such buckyball-type grains could not be explained either by theory of elastic homogeneous shell buckling or by templating of pore by PEG aggregates. It is revealed that a threshold number of soft PEG rich zones on the shell are necessary to induce buckling. The relatively small elastic modulus of the soft zones induces buckling at various centers, resulting in buckyball type of grains. A theoretical approach toward the simulation of the inhomogeneous elastic shell under external pressure is quite a complex problem and needs further attention.

■ ASSOCIATED CONTENT

Supporting Information

IR spectra for noncalcined and calcined grains (for S2 specimens) are shown in Figures S1 and S2, respectively. The size distribution of silica NPs, as estimated by SANS analysis, is shown in Figure S3. The approximate positions of the different modes in the IR spectra and its assignment to a functional group have been depicted in Table S1. This material is available free of charge via the Internet at <http://pubs.acs.org>.

■ AUTHOR INFORMATION

Corresponding Author

*E-mail: jbahadur@barc.gov.in. Phone: +91-22-25594606. Fax: +91-22- 25505151.

■ ACKNOWLEDGMENTS

We thank Drs. Henrich Frielinghaus and Günter Goerigk, JCNS, Germany, for their help in SANS experiments at KWS-1 and KWS-3, respectively. J.B. and D.S. thankfully acknowledge the financial support [DST(S)/AKR/P087/10-11/673] received from Department of Science and Technology, India through S. N. Bose National Centre for Basic Science, Kolkata, India for neutron scattering work at JCNS, Germany.

■ REFERENCES

(1) Fernandez-Nieves, A.; Cristobal, G.; Garces-Chavez, V.; Spalding, G. C.; Dholakia, K.; Weitz, D. A. *Adv. Mater.* **2005**, *17*, 680.

(2) Shklyarevskiy, I. O.; Jonkheijm, P.; Christianen, P. C. M.; Shennig, A. P. H. J.; Meijer, E. W.; Henze, O.; Kilbinger, A. F. M.; Feast, W. J.; Guerso, A.; Del, Desvergne, J.-P.; Maan, J. C. *J. Am. Chem. Soc.* **2005**, *127*, 1112.

(3) van Dillen, T.; Polman, A.; van Kats, C. M.; van Blaaderen, A. *Appl. Phys. Lett.* **2003**, *83*, 4315.

(4) Yin, Y.; Lu, Y.; Gates, B.; Xia, Y. *J. Am. Chem. Soc.* **2001**, *123*, 8718.

(5) Manoharan, V. N.; Elsesser, M. T.; Pine, D. J. *Science* **2003**, *301*, 483.

(6) Johnson, P. M.; van Kats, C. M.; van Blaaderen, A. *Langmuir* **2005**, *21*, 11510.

(7) Zerrouki, D.; Rotenberg, B.; Abramson, S.; et al. *Langmuir* **2006**, *22*, 57.

(8) Dillen, T.; van Blaaderen, A.; van Polman, A. *Mater. Today* **2004**, *7* (7–8), 40.

(9) Liddel, C. M.; Summers, C. J. *Adv. Mater.* **2003**, *15*, 1715.

(10) Nanda, N. C.; Schlieff, R., Eds. In *Advances in Echo Imaging Using Contrast Enhancement*; Kluwer Academic Publishers: Dordrecht, 1993.

(11) Marmottant, P.; Meer, S.; van der, Emmer, M.; Versluis, M.; Jong, N.; de; Hilgenfeldt, S.; Lohse, D. *J. Acoust. Soc. Am.* **2005**, *118*, 3499.

(12) Dinsmore, A. D.; Hsu, M. F.; Nikolaidis, M. G.; Marquez, M.; Bausch, A. R.; Weitz, D. A. *Science* **2002**, *298*, 1006.

(13) Imhof, A.; Pine, D. J. *Nature* **1997**, *389*, 948.

(14) Kuncicky, D. M.; Velev, O. D. *Langmuir* **2008**, *24*, 1371.

(15) Millman, J. R.; Bhatt, K. H.; Prevo, B. G.; Velev, O. D. *Nat. Mater.* **2005**, *4*, 98.

(16) Roh, K.-H.; Martin, D. C.; Lahann, J. *Nat. Mater.* **2005**, *4*, 759.

(17) Velev, O. D.; Lenhoff, A. M.; Kaler, E. W. *Science* **2000**, *287*, 2240.

(18) Master, K. *Spray Drying Handbook*, 5th ed.; Longman Scientific & Technical: Harlow, England, 1991.

(19) Iskandar, F.; Mikrajuddin.; Okuyama, K. *Nano Lett.* **2002**, *2* (4), 389–392.

(20) Sen, D.; Spalla, O.; Taché, O.; Haltebourg, P.; Thill, A. *Langmuir* **2007**, *23*, 4296–4302.

(21) Sen, D.; Spalla, O.; Belloni, L.; Charpentier, T.; Thill, A. *Langmuir* **2006**, *22*, 3798–3806.

(22) Sen, D.; Melo, J. S.; Bahadur, J.; Mazumder, S.; Bhattacharya, S.; D'Souza, S. F.; Frielinghaus, H.; Goerigk, G.; Loidl, R. *Soft Matter* **2011**, *7*, 5423.

(23) Sen, D.; Mazumder, S.; Melo, J. S.; Khan, A.; Bhattacharya, S.; D'Souza, S. F. *Langmuir* **2009**, *25* (12), 6690–6695.

(24) Lyonnard, S.; Bartlett, J. R.; Sizgek, E.; Finnie, K. S.; Zemb, T.; Woolfrey, J. L. *Langmuir* **2002**, *18*, 10386–10397.

(25) Sen, D.; Melo, J. S.; Bahadur, J.; Mazumder, S.; Bhattacharya, S.; Ghosh, G.; Dutta, D.; D'Souza, S. F. *Eur. Phys. J. E* **2010**, *31*, 393–402.

(26) Sen, D.; Khan, A.; Bahadur, J.; Mazumder, S.; Sapra, B. K. *J. Colloid Interface Sci.* **2010**, *347*, 25–30.

(27) Lee, S. Y.; Gradon, L.; Janeczko, S.; Iskandar, F.; Okuyama, K. *ACS Nano* **2010**, *4* (8), 4717.

(28) Lee, S. Y.; Widiyastuti, W.; Iskandar, F.; Okuyama, K.; Grado, L. *Aerosol Sci. Technol.* **2009**, *43*, 1184–119.

(29) Bahadur, J.; Sen, D.; Mazumder, S.; Paul, B.; Khan, A.; Ghosh, G. *J. Colloid Interface Sci.* **2010**, *351*, 357.

(30) Bahadur, J.; Sen, D.; Mazumder, S.; Bhattacharya, S.; Frielinghaus, H.; Goerigk, G. *Langmuir* **2011**, *27*, 8404–8414.

(31) Ivanovska, I. L.; Pablo, P. J.; de; Ibarra, B.; Sgalari, G.; MacKintosh, F. C.; Carrascosa, J. L.; Schmidt, C. F.; Wuite, G. J. L. *Proc. Natl. Acad. Sci. U. S. A.* **2004**, *101*, 7600.

(32) Michel, J. P.; Ivanovska, I. L.; Gibbons, M. M.; Klug, W. S.; Knobler, C. M.; Wuite, G. J. L.; Schmidt, C. F. *Proc. Natl. Acad. Sci. U. S. A.* **2006**, *103*, 6184.

(33) Fery, A.; Weinkamer, R. *Polymer* **2007**, *48*, 7221.

(34) Spector, M. S.; Naranjo, E.; Chiruvolu, S.; Zasadzinski, J. A. *Phys. Rev. Lett.* **1994**, *73*, 2867.

(35) Saint-Jalmes, A.; Gallet, F. *Eur. Phys. J. B* **1998**, *2*, 489.

- (36) Schmidt, C. F.; Svoboda, K.; Lei, N.; Petsche, I. B.; Berman, L. E.; Safinya, C. R.; Grest, G. S. *Science* **1993**, *259*, 952.
- (37) Landau, L. D.; Lifshitz, E. M. *Theory of Elasticity*; Oxford: Pergamon, 1986.
- (38) Komura, S.; Lipowsky, R. *J. Phys. II* **1992**, *2*, 1563.
- (39) Witten, T. A.; Li, H. *Europhys. Lett.* **1993**, *23*, 51.
- (40) Schwarz, U. S.; Komura, S.; Safran, S. A. *Europhys. Lett.* **2000**, *50*, 762.
- (41) Pauchard, L.; Allain, C. *Europhys. Lett.* **2003**, *62* (6), 897–903.
- (42) Tsapis, N.; Dufresne, E. R.; Sinha, S. S.; Riera, C. S.; Hutchinson, J. W.; Mahadevan, L.; Weitz, D. A. *Phys. Rev. Lett.* **2005**, *94*, 018302.
- (43) Quilliet, C.; Zoldesi, C.; Riera, C.; Blaaderen, A.; van, Imhof, A. *Eur. Phys. J. E* **2008**, *27*, 13–20.
- (44) Vliegthart, G. A.; Gompper, G. *New J. Phys.* **2011**, *13*, 045020.
- (45) Li, B.; Jia, F.; Cao, Y.-P.; Feng, X.-Q.; Gao, H. *Phys. Rev. Lett.* **2011**, *106*, 234301.
- (46) Pauchard, L.; Couder, Y. *Europhys. Lett.* **2004**, *66*, 667–673.
- (47) Sugiyama, Y.; Larsen, R. J.; Kim, J.-W.; Weitz, D. A. *Langmuir* **2006**, *22*, 6024.
- (48) Cheow, W. S.; Li, S.; Hadinoto, K. *Chem. Eng. Res. Des.* **2010**, *8*, 673.
- (49) Sacanna, S.; Irvine, W. T. M.; Rossi, L.; Pine, D. J. *Soft Matter* **2011**, *7*, 1631.
- (50) <http://www.labultima.com/lu228.htm>, accessed on Sept 29, 2011.
- (51) Mazumder, S.; Sen, D.; Saravanan, T.; Vijayaraghavan, P. R. *J. Neutron Res.* **2001**, *9*, 39; *Curr. Sci.* **2001**, *81*, 257.
- (52) Frielinghaus, H.; et al. *JCNS Experimental Report 2007/2008*; http://www.jcns.info/src/report/sr2008_KWS1_new_PB3.pdf
- (53) Goerigk, G.; Varga, Z. *J. Appl. Crystallogr.* **2011**, *44*, 337.
- (54) Spalla, O.; Lyonard, S.; Testard, F. *J. Appl. Crystallogr.* **2003**, *36*, 338.
- (55) Snavely, D. L.; Dubsy, J. *J. Polym. Sci.: Part A: Polym. Chem.* **1996**, *34*, 2575–2579.
- (56) Martinez, J. R.; Ruiz, F.; Vorobiev, Y. V.; Perez-Robles, F.; Gonzalez-Hernandez, J. *J. Chem. Phys.* **1998**, *109*, 7511.
- (57) Matos, M. C.; Ilharco, L. M.; Almeida, R. M. *J. Non-Cryst. Solids* **1992**, *147&148*, 232–237.
- (58) Elimelech, H.; Avnir, D. *Chem. Mater.* **2008**, *20*, 2224–2227.
- (59) Rayleigh, L. *Proc. R. Soc. London, Ser. A* **1911**, *84*, 25.
- (60) Aitchison, J.; Brown, J. A. C. *The Lognormal Distribution*; Cambridge University Press: Cambridge, 1957.
- (61) Pedersen, J. S. *J. Appl. Crystallogr.* **1994**, *7*, 595.
- (62) Baxter, R. J. *J. Chem. Phys.* **1968**, *49*, 2770.
- (63) Regnaut, C.; Ravey, J. C. *J. Chem. Phys.* **1989**, *91*, 1211.
- (64) Menon, S. V. G.; Manohar, C.; Srinivasa, R., K. *J. Chem. Phys.* **1991**, *95*, 9186.
- (65) Kamibayashi, M.; Ogura, H.; Otsubo, Y. *Ind. Eng. Chem. Res.* **2006**, *45*, 6899–6905.